Control of Three-Phase PMSM Drive With Minimum Sensor Usage

Shaowei Ren, *Student Member, IEEE*, Hui Song, Ruihui Chen, Dianxun Xiao, *Member, IEEE*, Zheng Wang, *Senior Member, IEEE*, and Xueqing Wang, *Senior Member, IEEE*

***Abstract*—This article investigates the control of three-phase permanent magnet synchronous motor (PMSM) drives with minimum sensor usage. To minimize the number of required current sensors, the dual space vector modulations (SVMs) are proposed for phase current reconstruction, synchronously executing vector synthesis twice within a control period. Furthermore, combining the extended Kalman filter and the mathematical relationship between the dc-link voltage and rotor velocity, an integrated observer of position and voltage is developed. In this way, only one single current sensor is required for the control of PMSM. The proposed solution can significantly reduce both the cost and the volume of PMSM drives. Finally, experimental results are provided to validate the effectiveness of the proposed strategy.**

***Index Terms*—Integrated observer of position and voltage, low-cost permanent magnet synchronous motor (PMSM) drives, phase current reconstruction.**

I. Introduction

PMSM has gained a broad market due to its high efficiency, high power density and low torque ripple [1], [2], [3]. For most drive applications, reducing the cost and size of permanent magnet synchronous motor (PMSM) drives without compromising performance is a key objective [4]. At present, many solutions have been developed to achieve this goal, such as three-phase four-switches (TPFS) inverters, electrolytic capacitorless technologies, switched reluctance motors (SRMs) and sensor removal techniques.

TPFS inverters limit the cost by reducing the number of power switches from six to four. However, this topology increases current harmonics and torque ripples due to the fluctuations in the dc-link midpoint voltage [5], [6], [7]. The electrolytic capacitorless technologies can significantly reduce the cost and size of the motor drives, but they degrade system stability and lead to inevitable torque fluctuations [8], [9], [10]. SRM has a simple structure, which reduces both material and manufacturing costs. However, the application of SRM is seriously restricted by the shortcomings of low power density and high torque pulsation [11], [12], [13]. Sensor removal techniques usually limit the cost of motor drives by reducing the number of sensors and using the sensorless algorithm as an alternative with slight performance sacrifice. In general, sensor removal techniques are promising and attract wide attention. This article will focus on the control of three-phase PMSM drives with minimum sensor usage.

Typical motor drives employ two or three individual current sensors to measure the three-phase currents. Alternatively, the three-phase currents can be reconstructed from a single current sensor (SCS), significantly reducing hardware complexity and cost [14], [15], [16], [17], [18], [19], [20]. When using an SCS, multiple samples are required within one control period and the sampling process inherently takes up a certain amount of time. Consequently, the measurement dead zones should be considered to reduce the sampling error throughout the sampling process. Multiple current samples can be obtained either from multiple branches [14], [15] or from a single branch [16], [17], [18], [19], [20]. The former modifies the hardware structure to make multiple branches pass through a SCS, fully utilizing the durations of zero vectors by shifting sampling points to zero vector intervals. The latter, commonly implemented with a SCS on the dc link, is preferred due to its simple hardware structure. In this configuration, all phase currents pass through the SCS, making it a practical choice for current reconstruction. Switching-state phase shift (SSPS) is one of the most widely applied current reconstruction techniques in industrial applications due to its straightforward implementation, achieved by shifting the drive signals in measurement dead zones [18]. Lu et al. [19] employs several active vectors to compensate for the measurement dead zones. These vectors are used for three-phase current sampling, thereby enhancing the accuracy of reconstructed currents. Shen et al. [20] inserts the measurement voltage vectors at the midpoint of PWM signals for current reconstruction. This approach preserves the symmetry of modulation signals, effectively reducing current harmonics compared to SSPS.

Received 28 February 2025; revised 14 June 2025; accepted 21 July 2025. Date of publication 23 July 2025; date of current version 27 August 2025. This work was supported in part by National Natural Science Foundation of China under Grant 62303333 and in part by the Project of Hetao Shenzhen-Hong Kong Science and Technology Innovation Cooperation Zone under Grant HZQB-KCZYB-2020083. Recommended for publication by Associate Editor G. Scelba. *(Corresponding author: Xueqing Wang.)*

Shaowei Ren, Ruihui Chen, and Xueqing Wang are with the College of Electrical Engineering, Sichuan University, Chengdu 610065, China (e-mail: 20222230351@stu.scu.edu.cn; chenrh@stu.scu.edu.cn; xwang@scu.edu.cn).

Hui Song is with State Grid Yantai Power Supply Company, Yantai 264003, China (e-mail: ytdlxxgk@163.com).

Dianxun Xiao is with the Sustainable Energy and Environment Thrust, The Hong Kong University of Science and Technology, Guangzhou 511455, China, and also with HKUST Shenzhen-Hong Kong Collaborative Innovation Research Institute, Futian 518048, China (e-mail: dianxunxiao@ust.hk).

Zheng Wang is with the School of Electrical Engineering, Southeast University, Nanjing 210096, China (e-mail: zwang@eee.hku.hk).

Color versions of one or more figures in this article are available at https://doi.org/10.1109/TPEL.2025.3592220.

Digital Object Identifier 10.1109/TPEL.2025.3592220

On the other hand, it is a common trend for low-cost motor drives to replace the position sensor with a model-based position observer [21], [22], [23], [24], [25]. Ye and Yao [21] enhance conventional flux sliding-mode observer by considering the variations of motor parameters, thereby improving system stability and addressing parameter mismatching issues. Xu et al. [22] introduces a third-order extended state observer to estimate position and speed, effectively minimizing estimation errors caused by parametric and load torque variations. [23] applies finite-control-set model predictive control based on current errors, significantly reducing current ripple and noise across the entire speed range. To address estimation errors caused by sliding mode observers, Yin et al. [24] proposes a novel phase-lock loop combined with a band-pass filter to suppress the estimation error after the sliding mode observer. Yang et al. [25] optimizes the original fourth-order EKF by dividing it into two third-order filters, thereby reducing the computational complexity in sensorless control.

While many researchers have focused on reducing current and position sensors, a few studies explore the removal of voltage sensors using voltage observers. Salmasi et al. [26] applie a flux observer to estimate the dc-link voltage and utilizes adaptive laws to improve system stability. Teng et al. [27] integrate sliding mode control with model predictive control, effectively reducing ripple in the observed dc-link voltage while improving dynamic response. Teng et al. [28] establishe a novel sliding mode surface and combines it with model reference adaptive laws to observe the dc-link voltage, enhancing the system's robustness to parameter variations.

Some research works have successfully removed the position sensor and use one dc-link current sensor by combining the above-mentioned techniques [19], [29], [30]. However, they still require the dc-link voltage sensor, leaving room for further cost reduction. Therefore, this article studies the control of three-phase PMSM drive system with minimal sensor usage to further reduce the drive cost, which is targeted at cost-sensitive drive applications, such as household appliances. The proposed solution can effectively remove both position sensor and dc-link voltage sensor, requiring only one SCS for the PMSM drive. First, a novel current reconstruction method is proposed, which achieves algorithmic uniformity across different sectors by utilizing the proposed dual space vector modulations (SVMs). In the dead zones of different sectors, the proposed method directly synthesizes the required vectors from the perspective of space vector synthesis, offering a universal solution. Second, the mathematical relationship between $\alpha\beta$-axis voltages in and rotor velocity is derived according to the motor model. On this basis, an EKF-based integrated estimation method of both dc-link voltage and rotor position is proposed. Finally, the PMSM can be effectively controlled with a SCS.

The rest of this article is organized as follows: Section II concretizes the main circuit structure, sensor layout and the associated control framework. Section III presents the principles of current reconstruction and the details of the proposed dual SVMs. Section IV introduces the position and dc-link voltage observer based on EKF. Then, the experimental results presented in Section V verify the feasibility and effectiveness of the proposed strategy. Finally, Section VI concludes this article.

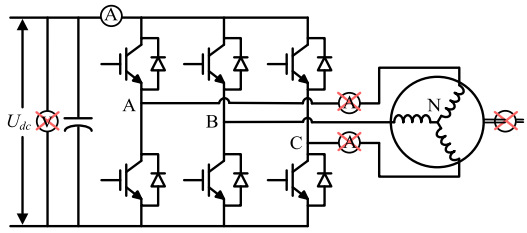

Fig. 1. PMSM drive with only one DC-link current sensor.

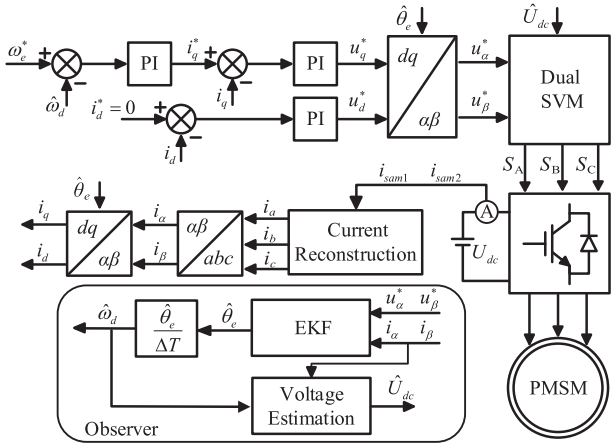

Fig. 2. Proposed control framework of PMSM drive with minimum sensor usage.

II. System Composition and Control Framework

A. System Composition

Fig. 1 shows the composition of the studied PMSM drive which only adopts a SCS in the dc link. No voltage or position sensors are used in the studied PMSM drive, minimizing the number of sensors from four to one. The low-cost current sampling solution, namely the combination of shunt resistor and operational amplifier, usually has a bandwidth higher than 1 MHz, which is sufficient for the dc-link current sampling of the PMSM drive with the switching frequency of 10 kHz in this article. On the other hand, the sampling noise of the current sensor during vector switching can be effectively filtered out by delaying the current sampling to the stable instant and precise current sampling can be guaranteed.

B. Proposed Control Framework

Fig. 2 illustrates the control framework of the studied PMSM drive shown in Fig. 1. In each control period, the dc-link current is sampled twice. Then, the required three-phase currents are reconstructed based on principles detailed in subsequent sections. Based on the PMSM model, EKF observer is established. In the observer, the reconstructed $\alpha\beta$-axis currents are used not only as input but also as feedback. Combined with the reference voltages generated from PI controllers, the position

TABLE I
RELATIONSHIP BETWEEN VOLTAGE VECTORS AND THE CURRENT SAMPLED BY A SINGLE DC-LINK CURRENT SENSOR

V_i	V_0	V_1	V_2	V_3	V_4	V_5	V_6	V_7
$S_AS_BS_C$	000	100	110	010	011	001	101	111
i_{sam}	0	i_a	$-i_c$	i_b	$-i_a$	i_c	$-i_b$	0

angle of the motor is ultimately observed. Then, the angular velocity is calculated from the angle by using the frequency measurement method. Finally, the estimated angular velocity and reconstructed $\alpha\beta$-axis currents are utilized together to estimate the dc-link voltage based on the motor model. In the proposed method, only one SCS is required for the control of PMSM drive and complete operating information of the PMSM drives can be obtained by using the proposed current reconstruction method and the proposed integrated observer of position and voltage. By comparison, the configuration of PMSM drive using a single dc-link voltage sensor or a single position sensor is not acceptable for practical applications due to the loss of current information. In general, the current sensor is necessary for the effective control of PMSM drive.

III. CURRENT RECONSTRUCTION

A. Current Reconstruction Principle

The dc-link current contains the information of three-phase currents which can be extracted based on different switching states, as given in Table I. V_i ($i = 01, \ldots, 7$) represents the voltage vectors. S_i ($i =$ A,B,C) represents for the switching state of each phase. i_{sam} is detected by the dc-link current sensor. During SVM, two different active vectors within a control period can be utilized for phase current sampling. For example, in sector-I, the active vectors $\boldsymbol{V_1}$ (100) and $\boldsymbol{V_2}$ (110) can be used to obtain the phase-A and phase-B currents respectively, which is expressed as

$$\begin{cases} i_{\text{sam1}} = i_a \\ i_{\text{sam2}} = -i_b \end{cases}. \tag{1}$$

Since the motor windings are star-connected, the third phase current can be calculated using the Kirchhoff's Current Law, which is expressed as

$$i_a + i_b + i_c = 0. \tag{2}$$

During dc-link current sampling, the active voltage vectors need to be maintained for sufficient duration to ensure current stabilization and obtain accurate sampled current. This minimum required duration, defined as $T_{\min}$, comprises four components: the dead time T_d of the inverter, the turn-ON delay T_{on} of power switches, the dc-link current settling time T_{set} for stabilization and the sampling window T_{sw} for effective analog-to-digital conversion, as expressed in

$$T_{\min} = T_d + T_{\text{on}} + T_{\text{set}} + T_{\text{sw}}. \tag{3}$$

Fig. 3 illustrates the distribution of various measurement dead zones in the space vector diagram. The sector boundary area

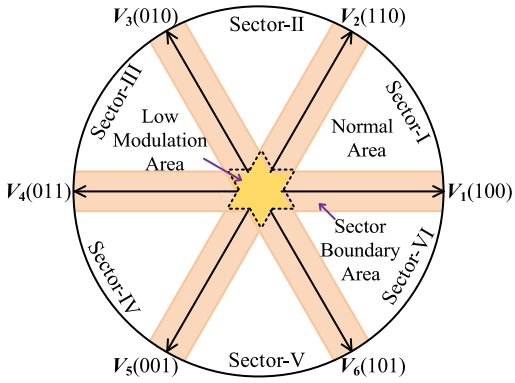

Fig. 3. Inverter output voltage-space-vector plane and unmeasurable areas.

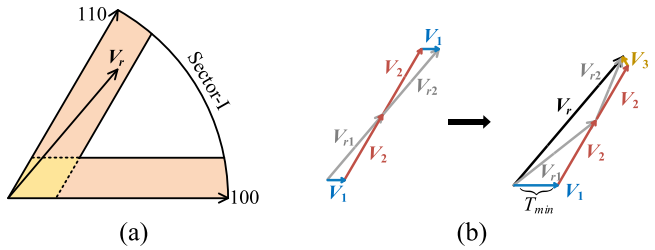

Fig. 4. Vector synthesis process in boundary area of sector-I. (a) Location of the reference vector. (b) Transformation from SVPWM to proposed dual SVMs.

occurs when the duration of a single active vector is less than $T_{\min}$, while the low modulation area appears when the durations of both two active vectors are less than $T_{\min}$.

B. Proposed Dual SVMs-Based Current Reconstruction

In traditional SVPWM, the modulated voltage vector is essentially a combination of two types of four active vectors and two types of zero vectors. The sampling of dc-link current only needs to be performed on two distinct active vectors. The proposed dual SVMs initially divides a control period T_s into two equal half periods $T_s/2$, equivalently splitting a complete reference vector $\boldsymbol{V_r}$ into two sub-reference vectors, $\boldsymbol{V_{r1}}$ and $\boldsymbol{V_{r2}}$. In this article, the two current sampling points are placed in the first half period. In Fig. 4, the length of each vector corresponds to its respective duration within the control period. When $\boldsymbol{V_r}$ enters the boundary dead zone of sector-I in Fig. 4(a), the duration of $\boldsymbol{V_1}$(100) generated by traditional SVPWM is difficult to meet the requirements of $T_{\min}$, resulting sampling error. By comparison, the duration of $\boldsymbol{V_1}$(100) in the proposed dual SVMs is extended to $T_{\min}$ in the first half period, while the duration of $\boldsymbol{V_2}$(110) remains unchanged, as shown in Fig. 4(b). Consequently, $\boldsymbol{V_{r2}}$ can be calculated by subtracting $\boldsymbol{V_{r1}}$ from $\boldsymbol{V_r}$. At this stage, $\boldsymbol{V_{r2}}$ may locate in sector-II, where it will be synthesized using the adjacent active vectors $\boldsymbol{V_2}$(110) and $\boldsymbol{V_3}$(010). The desired durations of active vectors can be directly obtained by synthesizing $\boldsymbol{V_{r1}}$ and $\boldsymbol{V_{r2}}$ independently in two half periods. The rest time in the modulation of two half periods is evenly distributed to two zero vectors, namely $\boldsymbol{V_0}$(000) and $\boldsymbol{V_7}$(111). When $\boldsymbol{V_r}$ lies within the normal area, the dual SVMs operates without requiring any modifications. In this area, the three-phase PWM waveforms

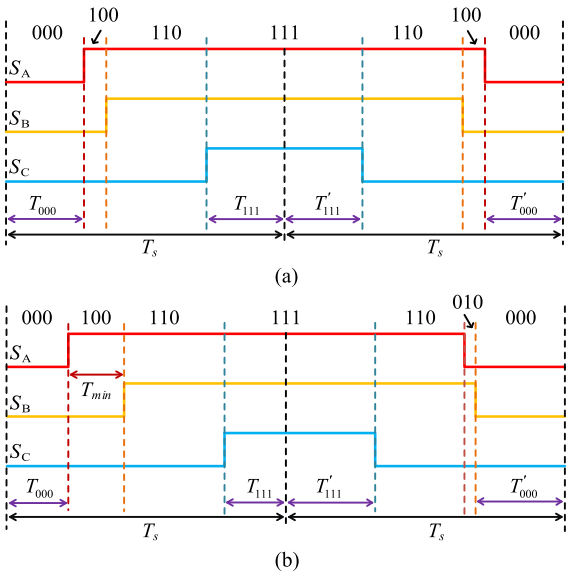

Fig. 5. Three-phase PWM waveforms in the boundary area of sector-I. (a) Conventional SVPWM. (b) Proposed dual SVMs.

generated by dual SVMs are consistent with those produced by traditional SVPWM.

Fig. 5 illustrates the three-phase PWM waveforms generated by the two kinds of space vectors modulations depicted in Fig. 4(b). In Fig. 5(a), the duration of $\boldsymbol{V_1}(100)$ is very short, which results in the sampling error of phase-A current. By using the proposed dual SVMs, the duration of $\boldsymbol{V_1}(100)$ in the first half period satisfies the requirement for $T_{\min}$, as shown in Fig. 5(b). Meanwhile, equal division of the zero vectors can be guaranteed, which contributes to lower harmonics.

Furthermore, the proposed dual SVMs improve the modulation range compared to SPSS. The modulation index m can be expressed as

$$m = \frac{\sqrt{3}|\boldsymbol{V_r}|}{U_{\rm dc}}. \tag{4}$$

In the classic SSPS method [18], the maximum modulation index M_S is given as

$$M_S = \begin{cases} 1, & T_{\min} \le 0.033T_s \\ \frac{2}{\sqrt{3}}\left(1 - \frac{4T_{\min}}{T_s}\right), & T_{\min} > 0.033T_s \end{cases}. \tag{5}$$

For the proposed dual SVMs, the maximum duration of active vectors before transformation is $T_s/2-T_{\min}$ per half period. This duration constraint differs from the SSPS, where the maximum duration is limited to $T_s/2-2T_{\min}$. Thus, the maximum modulation index M_D for the proposed dual SVMs is expressed as

$$M_D = \begin{cases} 1, & T_{\min} \le 0.067T_s \\ \frac{2}{\sqrt{3}}\left(1 - \frac{2T_{\min}}{T_s}\right), & T_{\min} > 0.067T_s \end{cases}. \tag{6}$$

Comparing (5) and (6), it can be found that M_D is improved by reducing the impact of $T_{\min}$.

The vector synthesis process of the proposed dual SVMs in the low modulation area follows the principle similar to that in

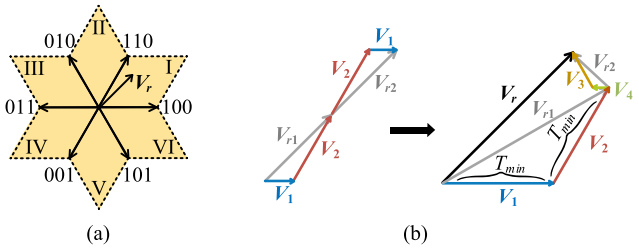

Fig. 6. Vector synthesis process in low modulation area of sector-I. (a) Location of the reference vector. (b) Transformation from SVPWM to dual SVMs.

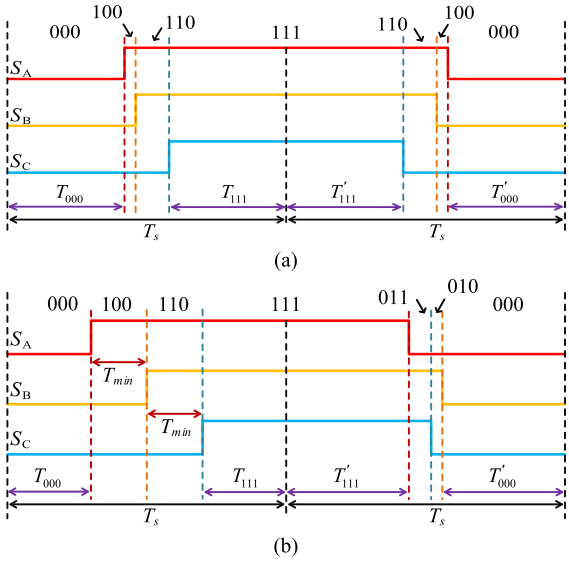

Fig. 7. Three-phase PWM waveforms in low modulation area of sector-I. (a) Conventional SVPWM. (b) Proposed dual SVMs.

the sector boundary area. The primary difference between them lies in the number of active vectors with durations shorter than $T_{\min}$. Taking the low modulation area of sector-I in Fig. 6(a) as an example, the durations of $\boldsymbol{V_1}(100)$ and $\boldsymbol{V_2}(110)$ generated by SVPWM are both shorter than the required $T_{\min}$. After applying dual SVMs, the durations of $\boldsymbol{V_1}(100)$ and $\boldsymbol{V_2}(110)$ are extended to $T_{\min}$ in the first half period, as shown in Fig. 6(b). $\boldsymbol{V_{r2}}$ is obtained by subtracting $\boldsymbol{V_{r1}}$ from $\boldsymbol{V_r}$. $\boldsymbol{V_{r2}}$ may extend beyond Sector-II and reside in Sector-III, in which case it will be synthesized using the adjacent active vectors $\boldsymbol{V_3}(010)$ and $\boldsymbol{V_4}(011)$. Similarly, the rest time of each half period is evenly distributed by two zero vectors. Fig. 7 illustrates the three-phase PWM waveforms of the conventional SVPWM and the proposed dual SVMs corresponding to Fig. 6(b). After applying dual SVMs, the durations of two active vectors in the first half period meet requirement $T_{\min}$, as shown in Fig. 7(b).

It can be concluded that the proposed dual SVMs feature a unified modulation modification process for both low-modulation and boundary measurement dead zones. The reference voltage vector is equally divided into two sub-reference vectors, with the PWM period correspondingly split into two half periods. The first subreference vector compensates the measurement dead zones while the second maintains equivalent total output voltage. The zero vectors are equally distributed in each half period. In

this way, the proposed dual SVMs can effectively reduce the algorithmic complexity and extend modulation range compared to the conventional SSPS method.

IV. Estimations of Position and DC-Link Voltage

A. Angle Estimation Based on EKF

According to the model of PMSM, the state space equation of the PMSM can be described as

$$\begin{cases} \dot{\boldsymbol{x}} = \boldsymbol{f}(\boldsymbol{x}) + \boldsymbol{B}\boldsymbol{u} \\ \boldsymbol{y} = \boldsymbol{C}\boldsymbol{x} \end{cases} \tag{7}$$

where

$$\boldsymbol{x} = \begin{bmatrix} i_\alpha & i_\beta & \omega_e & \theta_e \end{bmatrix}^T;\ \boldsymbol{u} = \begin{bmatrix} u_\alpha & u_\beta \end{bmatrix}^T;\ \boldsymbol{y} = \begin{bmatrix} i_\alpha & i_\beta \end{bmatrix}^T$$

$$\boldsymbol{B} = \begin{bmatrix} 1/L_s & 0 & 0 & 0 \\ 0 & 1/L_s & 0 & 0 \end{bmatrix}^T;\ \boldsymbol{C} = \begin{bmatrix} 1 & 0 & 0 & 0 \\ 0 & 1 & 0 & 0 \end{bmatrix}$$

$$\boldsymbol{f}(\boldsymbol{x}) = \begin{bmatrix} -\frac{R_s}{L_s} i_\alpha + \frac{\omega_e \psi_f}{L_s} \sin\theta_e \\ -\frac{R_s}{L_s} i_\beta - \frac{\omega_e \psi_f}{L_s} \cos\theta_e \\ 0 \\ \theta_e \end{bmatrix}$$

u_α, u_β, i_α and i_β are $\alpha\beta$-axis stator voltages and stator currents respectively; θ_e is electric angle of rotor; ω_e is electric angular velocity; R_s is stator resistance; L_s is stator inductance; and ψ_f is permanent-magnet flux linkage.

Then, (7) can be expressed in discrete form as

$$\begin{cases} \boldsymbol{x}_{k+1} = \boldsymbol{\Phi}_k \boldsymbol{x}_k + \boldsymbol{B}\boldsymbol{u}_k T_s \\ \boldsymbol{y}_{k+1} = \boldsymbol{C}\boldsymbol{x}_{k+1} \end{cases} \tag{8}$$

where $\boldsymbol{\Phi}_k = \boldsymbol{I} + T_s \frac{\partial \boldsymbol{f}(\boldsymbol{x})}{\partial \boldsymbol{x}}\big|_{\boldsymbol{x}=\hat{\boldsymbol{x}}_k}$

$$= \begin{bmatrix} 1 - \frac{R_s}{L_s} T_s & 0 & \frac{\psi_f}{L_s} T_s \sin\theta_{e(k)} & \frac{\omega_{e(k)} \psi_f}{L_s} T_s \cos\theta_{e(k)} \\ 0 & 1 - \frac{R_s}{L_s} T_s & -\frac{\psi_f}{L_s} T_s \cos\theta_{e(k)} & \frac{\omega_{e(k)} \psi_f}{L_s} T_s \sin\theta_{e(k)} \\ 0 & 0 & 1 & 0 \\ 0 & 0 & -T_s & 1 \end{bmatrix}$$

$\boldsymbol{I}$ is identity matrix.

Considering the model parameters error $\boldsymbol{w}$ and measurement error $\boldsymbol{v}$, the EKF observer is defined as

$$\begin{cases} \boldsymbol{x}_{k+1} = \boldsymbol{\Phi}_k \boldsymbol{x}_k + \boldsymbol{B}\boldsymbol{u}_k T_s + \boldsymbol{w}_k \\ \boldsymbol{y}_{k+1} = \boldsymbol{C}\boldsymbol{x}_{k+1} + \boldsymbol{v}_k \end{cases} \tag{9}$$

where both $\boldsymbol{w}$ and $\boldsymbol{v}$ are independent with each other and follow the rules of normal distribution: $\boldsymbol{w} \sim N(0, \boldsymbol{Q})$, $\boldsymbol{v} \sim N(0, \boldsymbol{R})$. The two matrices $\boldsymbol{Q}$ and $\boldsymbol{R}$ represent the variance of model noise and measurement noise, quantifying model and measurement uncertainties, respectively. $\boldsymbol{Q}$ and $\boldsymbol{R}$ are calculated from the maximum error of current sensor in the datasheet and the required estimation accuracy both through the probability density function of normal distribution.

The estimation process of the EKF observer is divided into two stages, namely the prediction stage and the update stage. In the prediction stage, the system states for the present control period are predicted based on the mathematical model and the estimated values from the previous period. In the update stage, the sampled phase currents from the present period are utilized to improve the prediction, thereby achieving optimal state estimation. The corresponding mathematical steps are as follows:

1) *Prediction:* Based on $\hat{\boldsymbol{x}}_k^+$ and the discrete mathematical model (9), $\hat{\boldsymbol{x}}_{k+1}^-$ at the next period can be directly computed as

$$\hat{\boldsymbol{x}}_{k+1}^- = \boldsymbol{\Phi}_k \hat{\boldsymbol{x}}_k^+ + \boldsymbol{B}\boldsymbol{u}_k T_s. \tag{10}$$

The prior covariance P_k^- is need to be prepared for the subsequent update stage. The formula for its calculation is presented as

$$\boldsymbol{P}_{k+1}^- = \boldsymbol{\Phi}_k \boldsymbol{P}_k^+ \boldsymbol{\Phi}_k^T + \boldsymbol{Q} \tag{11}$$

where $\boldsymbol{u}_k^* = \begin{bmatrix} u_{\alpha(k)}^* & u_{\beta(k)}^* \end{bmatrix}^T$, which are $\alpha\beta$-axis reference voltages generated by the control system in the (k)th period; $\hat{\boldsymbol{x}}_k^-$ is the priori state estimation; $\hat{\boldsymbol{x}}_k^+$ is the posterior state estimation; $\boldsymbol{P}_k^-$ is prior covariance; and $\boldsymbol{P}_k^+$ is the posterior covariance.

2) *Update:* feedback correction is applied to the predicted $\hat{\boldsymbol{x}}_{k+1}^-$ to obtain the optimal estimation $\hat{\boldsymbol{x}}_{k+1}^+$

$$\hat{\boldsymbol{x}}_{k+1}^+ = \hat{\boldsymbol{x}}_{k+1}^- + \boldsymbol{K}_{k+1}\left(\boldsymbol{y}_{k+1} - \boldsymbol{C}\hat{\boldsymbol{x}}_{k+1}^-\right). \tag{12}$$

The Kalman gain matrix $\boldsymbol{K}_{k+1}$ can be calculated as

$$\boldsymbol{K}_{k+1} = \frac{\boldsymbol{P}_{k+1}^- \boldsymbol{C}^T}{\boldsymbol{C}\boldsymbol{P}_{k+1}^- \boldsymbol{C}^T + \boldsymbol{R}}. \tag{13}$$

Posterior covariance $\boldsymbol{P}_k^+$ needs to be updated for next iteration, which is expressed as

$$\boldsymbol{P}_{k+1}^+ = \left(\boldsymbol{I} - \boldsymbol{K}_{\mathrm{k}+1}\boldsymbol{C}\right)\boldsymbol{P}_{k+1}^-. \tag{14}$$

Finally, the rotor angle represented in the state variable can be accurately estimated through the above process.

B. Angular Velocity Estimation

Although the angular velocity can be estimated though the above process, its value may not perfectly match the real velocity. The mismatch is primarily caused by the difference between the reference voltages and the real inverter output voltages.

Neglecting the voltage drop in the motor windings, the back electromotive force is approximately equal to the real inverter output voltage. The motor model in (7) can be simplified as

$$\begin{cases} u_{\alpha\_rl} \approx -\omega_{rl} \psi_f \sin\hat{\theta}_e \\ u_{\beta\_rl} \approx \omega_{rl} \psi_f \cos\hat{\theta}_e \end{cases}. \tag{15}$$

Then, the voltage errors between the real inverter output voltages and the reference voltages can be expressed as

$$\begin{cases} \Delta u_\alpha = u_{\alpha\_rl} - u_\alpha^* \approx -\left(\omega_{rl} - \hat{\omega}_e\right)\psi_f \sin\hat{\theta}_e \\ \Delta u_\beta = u_{\beta\_rl} - u_\beta^* \approx \left(\omega_{rl} - \hat{\omega}_e\right)\psi_f \cos\hat{\theta}_e \end{cases} \tag{16}$$

where u_{α_rl} and u_{β_rl} are the real $\alpha\beta$-axis voltages of the inverter; Δu_α and Δu_β are the voltage errors; ω_{rl} is the real angular velocity of motor; $\hat{\omega}_e$ and $\hat{\theta}_e$ are the estimated angular velocity and angle from the EKF observer.

For better understanding the impact of voltage error on angular velocity estimation, (16) can be rewritten as

$$\Delta U_{\alpha\beta} \approx \Delta\omega_e \psi_f \tag{17}$$

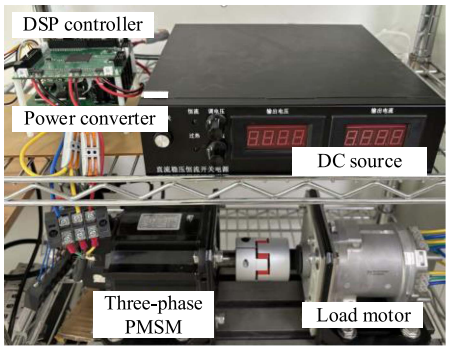

Fig. 8. Experimental platform.

TABLE II
EXPERIMENTAL PARAMETERS

Parameter	Value
d-axis inductance	7.5 mH
q-axis inductance	7.5 mH
Stator resistance	0.5 Ω
PM flux linkage	0.072 Wb
Pole pair	5
Rated current	7 A
Rated speed	600 r/min
Rated load torque	5.3 N·m
Control frequency	10 kHz

where $\Delta U_{\alpha\beta} = \sqrt{\Delta u_\alpha{}^2 + \Delta u_\beta{}^2}$, $\Delta\omega_e = \omega_{rl} - \hat{\omega}_e$.

According to (17), the voltage error primarily contributes to an estimation error of angular velocity in EKF observer, exhibiting an approximately linear relationship. Consequently, $\hat{\omega}_e$derived from the EKF observer should not be directly employed as a feedback variable in the control system. By comparison, differentiating the angle provides an accurate estimation of angular velocity. In discrete form, the specific angular velocity is expressed as

$$\hat{\omega}_d = \frac{\Delta\hat{\theta}_e}{\Delta T} \tag{18}$$

where the time interval ΔT can be set as a multiple of the control period T_s and $\Delta\hat{\theta}_e$ is the angle difference during this interval.

C. DC-Link Voltage Estimation

Given the control objective of $i_d = 0$, the α-axis and β-axis currents can be simplified as

$$\begin{cases} i_\alpha = -I\sin\theta_e \\ i_\beta = I\cos\theta_e \end{cases} \tag{19}$$

where I is the amplitude of the sampled phase currents.

By substituting (19) into (7), the voltage equation in (7) can be rewritten as

$$\begin{cases} \hat{u}_\alpha = -(R_s I + \hat{\omega}_d\psi_f)\sin(\hat{\theta}_e) - L_s I\hat{\omega}_d\cos(\hat{\theta}_e) \\ \hat{u}_\beta = (R_s I + \hat{\omega}_d\psi_f)\cos(\hat{\theta}_e) - L_s I\hat{\omega}_d\sin(\hat{\theta}_e) \end{cases} \tag{20}$$

where $\hat{u}_\alpha$ and $\hat{u}_\beta$ are the estimated $\alpha\beta$-axis voltages of the inverter.

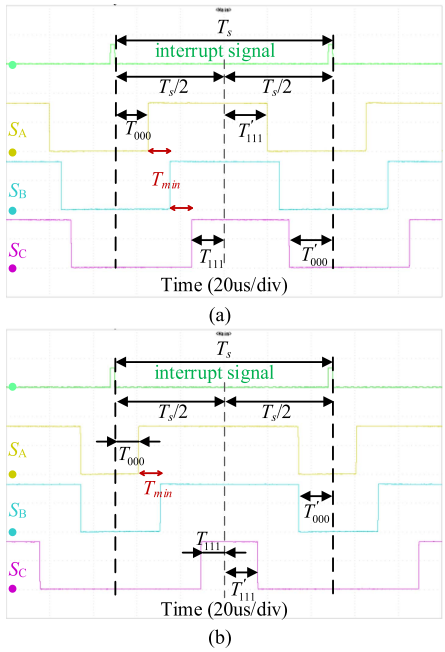

Fig. 9. Three-phase PWM waveforms of the proposed dual SVMs in different modulation indices. (a) $m = 0.1$. (b) $m = 0.8$.

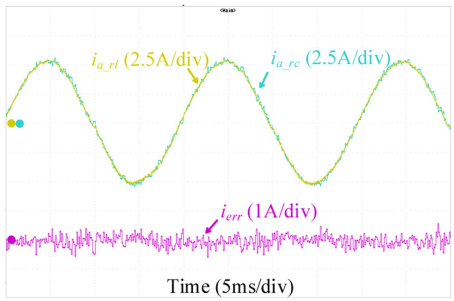

Fig. 10. Current reconstruction using the proposed dual SVMs at the speed of 600 r/min.

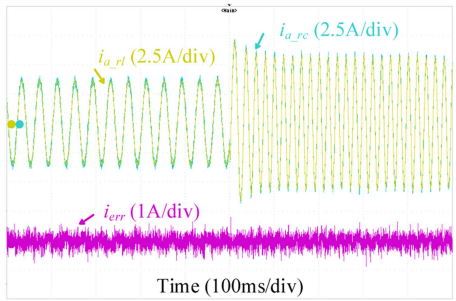

Fig. 11. Current reconstruction using the proposed dual SVMs with a speed step from 300 to 600 r/min.

Based on (20), the amplitude of the estimated $\alpha\beta$-axis voltage can be expressed as

$$\hat{U}_{\alpha\beta} = \sqrt{\hat{u}_\alpha^2 + \hat{u}_\beta^2} = \sqrt{(L_s I\hat{\omega}_d)^2 + (R_s I + \hat{\omega}_d\psi_f)^2}. \tag{21}$$

The ratio between the amplitude of the reference voltages $U^*_{\alpha\beta}$ and the dc-link voltage is determined within a control period. Therefore, the dc-link voltage can be estimated by using this

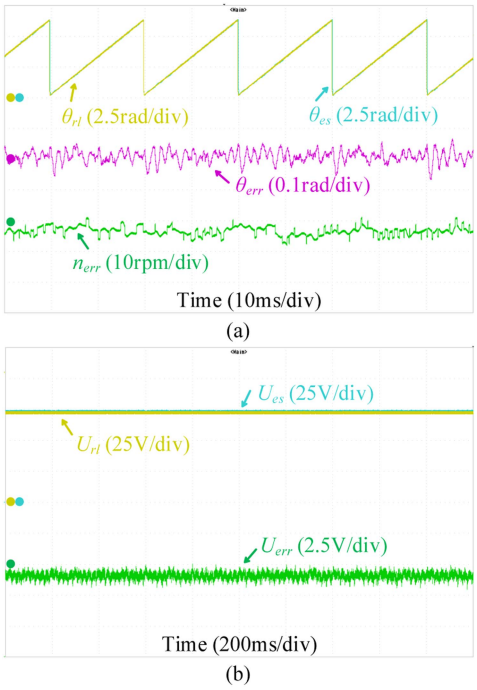

Fig. 12. Observations of position and DC-link voltage at the speed of 600 r/min. (a) Real angle θ_{rl}, estimated angle θ_{es}, estimated angle error $\theta_{\rm err}$, and speed error $n_{\rm err...}$ (b) Real DC-link voltage U_{rl}, estimated DC-link voltage U_{es} and DC-link voltage error $U_{\rm err}$.

ratio with the known value of $\hat{U}_{\alpha\beta}$, which is expressed as

$$\hat{U}_{\rm dc(k+1)} = \frac{\hat{U}_{\alpha\beta}}{U^*_{\alpha\beta}} \hat{U}_{\rm dc(k)} \tag{22}$$

where $U^*_{\alpha\beta} = \sqrt{u^{*2}_{\alpha} + u^{*2}_{\beta}}$; $\hat{U}_{\rm dc}$ represents the estimation of dc-link voltage. Finally, the estimated dc-link voltage will participate in the modulation.

It should be noted that the inverter nonlinearity will increase the estimation errors of both position and dc-link voltage. The common compensation methods for inverter nonlinearity can be directly introduced into the proposed strategy to improve the estimation precision [31].

V. Experimental Verification

To verify the effectiveness of the proposed low-cost control strategy for three-phase PMSM drives with minimal sensor usage, an experimental platform is established as shown in Fig. 8. The experimental platform includes a DSP controller (TMS320F28377), a dc source, a power converter and a controlled PMSM and a load PMSM. Besides, a dc-link voltage sensor, three current sensors and an encoder are equipped to obtain the corresponding real values to prove the accuracy of the proposed strategy. The primary parameters of the experimental platform are provided in Table II.

Fig. 9 presents the three-phase PWM waveforms of the proposed dual SVMs under different modulation indices. The falling edge of the interrupt signal indicates the start of the control period. The minimum active vector duration $T_{\rm min}$ is set

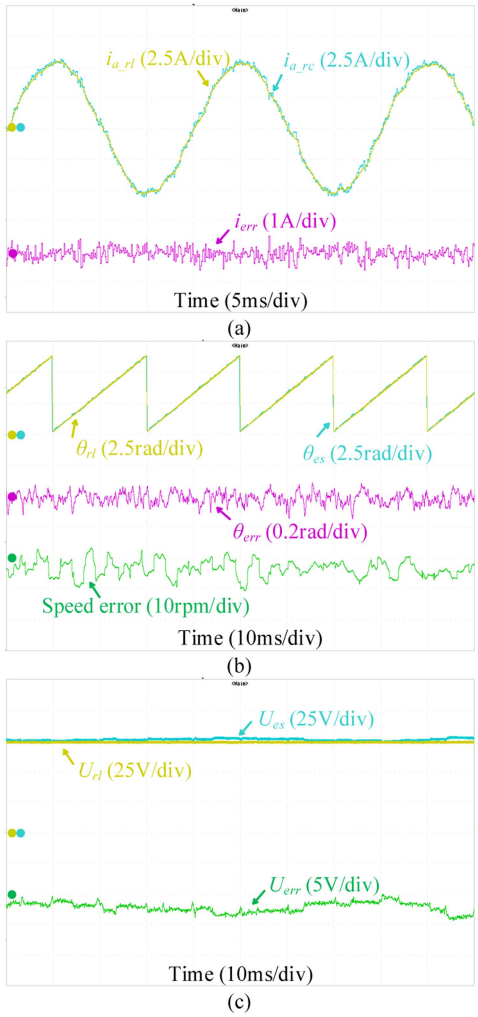

Fig. 13. Steady-state experiments with minimum sensor usage at the speed of 600 r/min. (a) Real phase-A current i_{a_rl}, reconstructed phase-A current i_{a_rc} and reconstructed current error $i_{\rm err}$. (b) Real angle θ_{rl}, estimated angle θ_{es}, estimated angle error $\theta_{\rm err}$ and speed error $n_{\rm err}$. (c) Real DC-link voltage U_{rl}, estimated DC-link voltage U_{es} and estimated voltage error $U_{\rm err}$.

to 10 us. The current sampling is triggered 2 us before the vector switching instant through a PWM-generated interrupt. This parameter configuration ensures sufficient current settling time for better sampling accuracy. As demonstrated in the theoretical analysis, the durations of zero vectors are evenly divided within each half cycle, contributing to lower harmonics.

Fig. 10 presents the experimental results of current reconstruction using the proposed dual SVMs at the speed of 600 r/min. Although some distortion exists in the phase-A current reconstructed from the dc-link current i_{a_rc}, the real Phase-A current i_{a_rl} remains smooth with low current harmonics at 4.89%. The maximum current error $i_{\rm err}$ between them is 0.5 A, demonstrating the effectiveness of the proposed dual SVMs. In Fig. 11, the experimental results of current reconstruction using the proposed dual SVMs is further conducted during a speed step from 300 to 600 r/min. During the transition, the reconstructed current maintains consistently low error levels, demonstrating that the current reconstruction using the proposed dual SVMs exhibits strong robustness under dynamic operating conditions.

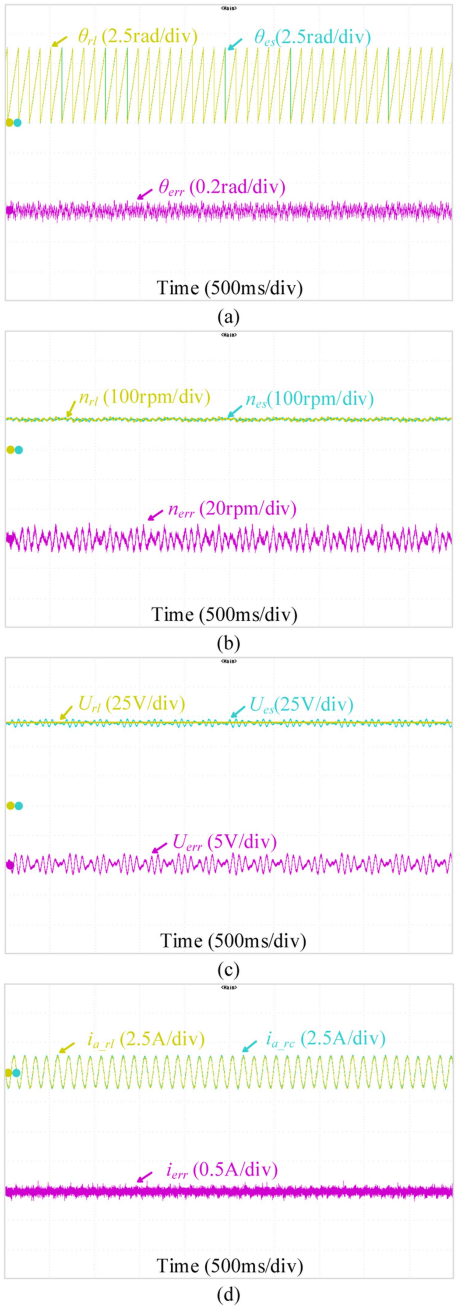

Fig. 14. Steady-state experiments with minimum sensor usage at a low speed of 100 r/min. (a) Real angle θ_{rl}, estimated angle θ_{es} and angle error $\theta_{\rm err}$. (b) Real speed n_{rl}, estimated speed n_{es} and speed error $n_{\rm err}$. (c) Real DC-link voltage U_{rl}, estimated DC-link voltage U_{es} and DC-link voltage error U_{err}. (d) Real phase-A current i_{a_rl}, reconstructed phase-A current i_{a_rc} and reconstructed current error $i_{\rm err}$.

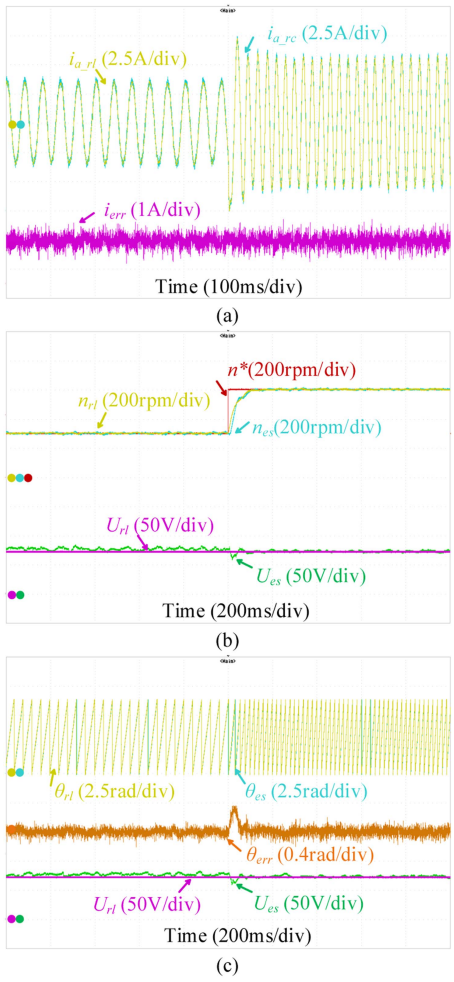

Fig. 15. Dynamic experiments with minimum sensor usage from 300 to 600 r/min. (a) Real phase-A current i_{a_rl}, reconstructed phase-A current i_{a_rc} and reconstructed current error $i_{\rm err}$. (b) Real speed n_{rl}, estimated speed n_{es}, reference speed n^*, real DC-link voltage U_{rl} and estimated DC-link voltage U_{es}. (c) Real angle θ_{rl}, estimated angle θ_{es}, estimated angle error $\theta_{\rm err}$, real DC-link voltage U_{rl} and estimated DC-link voltage U_{es}.

Since the current ripple in Fig. 11 is primarily caused by the sampling noise of the current sensor, it is almost unaffected by the current magnitude.

Fig. 12 presents the experimental results of the position and voltage observer at the speed of 600 r/min without using current reconstruction. In Fig. 12(a), the estimated angle almost coincides with the real angle with a maximum angle error below 0.1 rad. The speed error is maintained below 8 r/min, corresponding to a relative error of less than 2%. Fig. 12(b) presents the estimated result of the dc-link voltage, where the magnitude of the error between the real and estimated dc-link voltages fluctuates within ± 1 V. The small dc offset in Fig. 12(b) between the estimated and the real voltages is caused by the inverter nonlinearity and can be eliminate by compensating the inverter nonlinearity.

The comprehensive experimental results combining current reconstruction with integrated observer of position and voltage are presented in Figs. 13–18. Only one dc-link current sensor is used. Fig. 13 presents the steady-state experiments with minimum sensor usage at the speed of 600 r/min. Although some distortion exists in the real phase currents, it does not affect the accuracy of reconstructed currents in Fig. 13(a). The current reconstruction error still remains below 0.5 A. In Fig. 13(b) and (c), both the rotor position and the dc-link voltage can be precisely estimated. In Fig. 13(c), the dc-link voltage error exhibits a small dc bias which is jointly caused by the motor parameter mismatch and inverter nonlinearity.

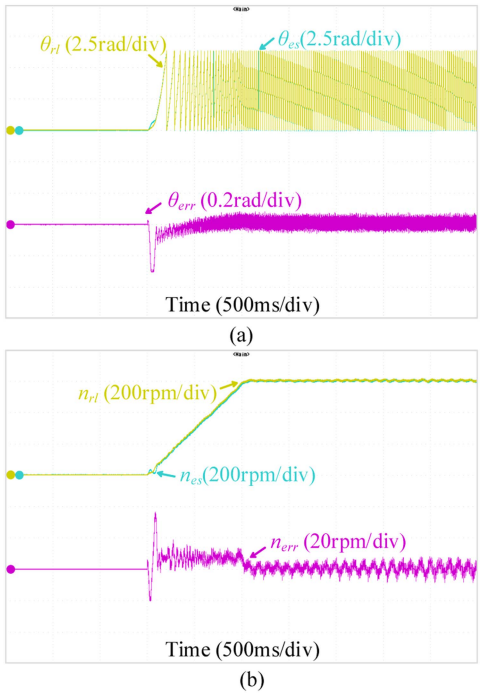

Fig. 16. Start-up experiments with minimum sensor usage from zero speed to 600 r/min. (a) Real angle θ_{rl}, estimated angle θ_{es}, and angle error θ_{err}. (b) Real speed n_{rl}, estimated speed n_{es}, and speed error n_{err}.

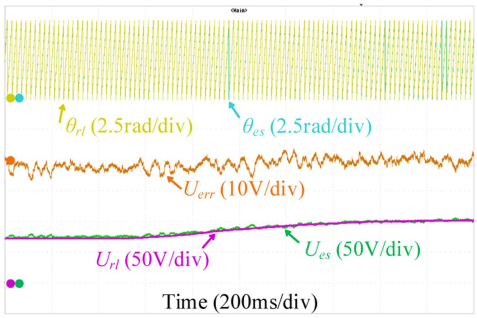

Fig. 17. Experimental results with minimum sensor usage during the transition of real DC-link voltage from 70 to 100 V.

Fig. 14 shows the experimental results with minimum sensor usage at a low speed of 100 r/min. In low-speed operation, the estimation error of the integrated observer will be slightly increased than that in other speeds due to the low back electromotive force, as shown in Fig. 14(a)–(c). Meanwhile, the estimated speed and dc-link voltage contain some low-frequency fluctuations which are acceptable for stable operation. The precision of current reconstruction will not be affected speed, as shown in Fig. 14(d).

Fig. 15 presents the speed response experiments with minimum sensor usage from 300 to 600 r/min. In Fig. 15(a), the phase currents can be quickly and accurately reconstructed in both steady and transient states. In Fig. 15(b), both the real and estimated speeds can effectively track the changing reference speed. In Fig. 15(c), the estimated angle closely aligns with the real value. During acceleration, the angle error is slightly increased and eliminated in short time. Meanwhile, the estimated

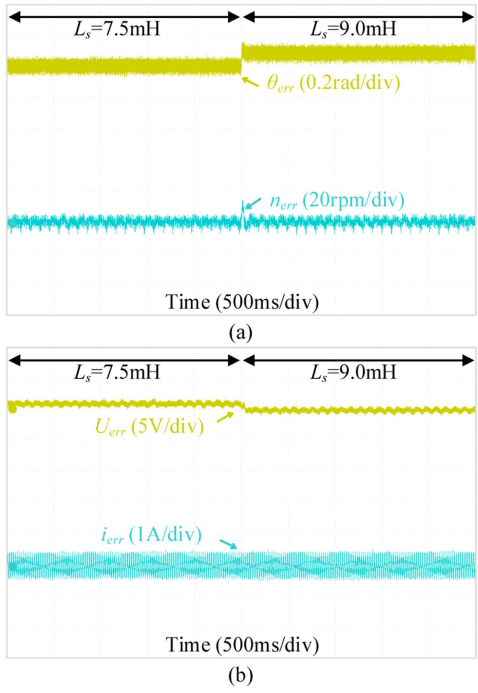

Fig. 18. Inductance parameter mismatch experiments with minimum sensor usage. (a) Angle error θ_{err} and speed error n_{err}. (b) DC-link voltage error U_{err} and reconstructed current error i_{err}.

dc-link voltage experiences a small drop due to the increased angle error. The increased angle and voltage estimation errors during dynamic operation can be relieved by reducing the system model error and time delay. Since the estimation errors in Fig. 15 still remains well within the stability margin, they are acceptable for practical applications. Fig. 16 shows the start-up experiments with minimum sensor usage from zero speed to 600 r/min. During the start-up process, although a certain estimation delay exists in the position and speed, the increased estimation error during dynamic operation is relatively small and the motor can still achieve smooth acceleration.

Fig. 17 shows the experimental results with minimum sensor usage during the transition of real dc-link voltage from 70 to 100 V at the speed of 600 r/min. During the change of real dc-link voltage, the estimated dc-link voltage can accurately track the real dc-link voltage. The estimated voltage error remains virtually unchanged and no fluctuation occurs in both estimated and real angles, indicating the effective of the observer in dynamic process.

Fig. 18 shows the impact of parameter mismatch on the estimation and reconstruction errors. The stator inductance L_s in the integrated observer is changed from 7.5 to 9 mH with an inductance mismatch error of 20%. Since the integrated observer of position and voltage relies on the motor parameters, the parameter mismatch will slightly increase the errors of both position and dc-link voltage, as shown in Fig. 18(a) and (b). On the other hand, the precisions of speed estimation and current reconstruction are not affected by the parameter change. In general, the increase the errors of position and dc-link voltage caused by parameter mismatch are acceptable for stable operation.

VI. Conclusion

This article proposes a low-cost control strategy for three-phase PMSM drives with minimum sensor usage. To reduce the number of current sensors, a dual-SVMs method based current reconstruction is proposed. This method synthesizes the required vectors from the perspective of space vectors. The synthesis process of the two subvectors is similar and there is no need to account for the differences in measurement dead zones across different sectors, which simplifies the implementation. The durations of the zero vectors in each adjacent period are nearly equal, which contributes to lower harmonics. Additionally, based on the mathematical model of PMSM, an EKF-based state observer is developed to estimate both the rotor angle and the dc-link voltage effectively. Finally, by integrating the current reconstruction with the observer, the entire system is controlled using only one dc-link current sensor, significantly reducing system costs while ensuring stable motor control performance.

References

[1] Q. Wang, X. Zhao, P. Yang, W. Hua, and G. Buja, "Effects of triangular wave injection and current differential terms on multiparameter identification for PMSM," *IEEE Trans. Power Electron.*, vol. 39, no. 3, pp. 2943–2947, Mar. 2024.

[2] D. Ma, X. Wang, D. Xiao, X. Yan, Y. Liu, and Z. Wang, "High-precision modulation strategy for hybrid inverters based OW-PMSM drives," *IEEE J. Emerg. Sel. Topics. Power Electron.*, vol. 13, no. 1, pp. 1158–1167, Feb. 2025.

[3] L. Zhang, M. Zhang, X. Zhu, Z. Pei, and X. Chen, "Space decoupling sensorless control of five-phase flux-intensifying PM motor based on AFCCF-SMO considering flux-weakening operation," *IEEE Trans. Ind. Electron.*, vol. 72, no. 7, pp. 6865–6875, Jul. 2025.

[4] G. Wang, M. Valla, and J. Solsona, "Position sensorless permanent magnet synchronous machine drives—A review," *IEEE Trans. Ind. Electron.*, vol. 67, no. 7, pp. 5830–5842, Jul. 2020.

[5] C. Zhu, Z. Zeng, and R. Zhao, "Comprehensive analysis and reduction of torque ripples in three-phase four-switch inverter-fed PMSM drives using space vector pulse-width modulation," *IEEE Trans. Power Electron.*, vol. 32, no. 7, pp. 5411–5424, Jul. 2017.

[6] D. Zhou, J. Zhao, and Y. Liu, "Predictive torque control scheme for three-phase four-switch inverter-fed induction motor drives with DC-link voltages offset suppression," *IEEE Trans. Power Electron.*, vol. 30, no. 6, pp. 3309–3318, Jun. 2015.

[7] Z. Li, J. Xia, X. Gao, J. Rodriguez, Y. Guo, and X. Zhang, "Modulated model predictive torque control for fault-tolerant inverter-fed induction motor drives with single DC-link voltage sensor," *IEEE Trans. Power Electron.*, vol. 38, no. 7, pp. 8798–8810, Jul. 2023.

[8] N. Zhao, G. Wang, D. Xu, and D. Xiao, "An active damping control method for reduced DC-link capacitance IPMSM drives," *IEEE Trans. Ind. Electron.*, vol. 65, no. 3, pp. 2057–2068, Mar. 2018.

[9] D. Ding, G. Wang, N. Zhao, G. Zhang, and D. Xu, "An anti-overvoltage control scheme for electrolytic capacitorless IPMSM drives based on stator current vector orientation," *IEEE Trans. Ind. Electron.*, vol. 67, no. 5, pp. 3517–3527, May 2020.

[10] N. Zhao, G. Wang, B. Li, R. Zhang, and D. Xu, "Beat phenomenon suppression for reduced DC-link capacitance IPMSM drives with fluctuated load torque," *IEEE Trans. Ind. Electron.*, vol. 66, no. 11, pp. 8334–8344, Nov. 2019.

[11] E. Bostanci, M. Moallem, A. Parsapour, and B. Fahimi, "Opportunities and challenges of switched reluctance motor drives for electric propulsion: A comparative study," *IEEE Trans. Transp. Electrific.*, vol. 3, no. 1, pp. 58–75, Mar. 2017.

[12] V. P. Vujičić, "Minimization of torque ripple and copper losses in switched reluctance drive," *IEEE Trans. Power Electron.*, vol. 27, no. 1, pp. 388–399, Jan. 2012.

[13] J. Ye, B. Bilgin, and A. Emadi, "An extended-speed low-ripple torque control of switched reluctance motor drives," *IEEE Trans. Power Electron.*, vol. 30, no. 3, pp. 1457–1470, Mar. 2015.

[14] Q. Tang, A. Shen, W. Li, P. Luo, M. Chen, and X. He, "Multiple-positions-coupled sampling method for PMSM three-phase current reconstruction with a single current sensor," *IEEE Trans. Power Electron.*, vol. 35, no. 1, pp. 699–708, Jan. 2020.

[15] Y. Xu, H. Yan, J. Zou, B. Wang, and Y. Li, "Zero voltage vector sampling method for PMSM three-phase current reconstruction using single current sensor," *IEEE Trans. Power Electron.*, vol. 32, no. 5, pp. 3797–3807, May 2017.

[16] J.-I. Ha, "Voltage injection method for three-phase current reconstruction in PWM inverters using a single sensor," *IEEE Trans. Power Electron.*, vol. 24, no. 3, pp. 767–775, Mar. 2009.

[17] H. Lu, X. Cheng, W. Qu, S. Sheng, Y. Li, and Z. Wang, "A three-phase current reconstruction technique using single DC current sensor based on TSPWM," *IEEE Trans. Power Electron.*, vol. 29, no. 3, pp. 1542–1550, Mar. 2014.

[18] Y. Gu, F. Ni, D. Yang, and H. Liu, "Switching-state phase shift method for three-phase-current reconstruction with a single DC-link current sensor," *IEEE Trans. Ind. Electron.*, vol. 58, no. 11, pp. 5186–5194, Nov. 2011.

[19] J. Lu, X. Zhang, Y. Hu, J. Liu, C. Gan, and Z. Wang, "Independent phase current reconstruction strategy for IPMSM sensorless control without using null switching states," *IEEE Trans. Ind. Electron.*, vol. 65, no. 6, pp. 4492–4502, Jun. 2018.

[20] Y. Shen, Z. Zheng, Q. Wang, P. Liu, and X. Yang, "DC bus current sensed space vector pulsewidth modulation for three-phase inverter," *IEEE Trans. Transp. Electrific.*, vol. 7, no. 2, pp. 815–824, Jun. 2021.

[21] S. Ye and X. Yao, "A modified flux sliding-mode observer for the sensorless control of PMSMs with online stator resistance and inductance estimation," *IEEE Trans. Power Electron.*, vol. 35, no. 8, pp. 8652–8662, Aug. 2020.

[22] Z. Xu, T. Zhang, Y. Bao, H. Zhang, and C. Gerada, "A nonlinear extended state observer for rotor position and speed estimation for sensorless IPMSM drives," *IEEE Trans. Power Electron.*, vol. 35, no. 1, pp. 733–743, Jan. 2020.

[23] Z. Chen, J. Qiu, and M. Jin, "Prediction-error-driven position estimation method for finite-control-set model predictive control of interior permanent-magnet synchronous motors," *IEEE J. Emerg. Sel. Topics. Power Electron.*, vol. 7, no. 1, pp. 282–295, Mar. 2019.

[24] Z. Yin, Y. Zhang, X. Cao, D. Yuan, and J. Liu, "Estimated position error suppression using novel PLL for IPMSM sensorless drives based on full-order SMO," *IEEE Trans. Power Electron.*, vol. 37, no. 4, pp. 4463–4474, Apr. 2022.

[25] H. Yang, R. Yang, W. Hu, and Z. Huang, "FPGA-based sensorless speed control of PMSM using enhanced performance controller based on the reduced-order EKF," *IEEE J. Emerg. Sel. Top. Power Electron.*, vol. 9, no. 1, pp. 289–301, Feb. 2021.

[26] F. R. Salmasi, T. A. Najafabadi, and P. J. Maralani, "An adaptive flux observer with online estimation of DC-link voltage and rotor resistance for VSI-based induction motors," *IEEE Trans. Power Electron.*, vol. 25, no. 5, pp. 1310–1319, May 2010.

[27] Q. Teng, H. Yang, and J. Tian, "Nonlinear function integral sliding mode-based model predictive current control for PMSM drives with DC-bus voltage observer," *CPSS Trans. Power Electron. Appl.*, vol. 7, no. 4, pp. 399–408, Dec. 2022.

[28] Q. Teng, J. Tian, J. Duan, H. Cui, J. Zhu, and Y. Guo, "Sliding-mode MRA observer-based model predictive current control for PMSM drive system with DC-link voltage sensorless," in *Proc. 20th Int. Conf. Elect. Mach. Syst.*, 2017, pp. 1–6.

[29] J. Zhao, S. Nalakath, and A. Emadi, "A high frequency injection technique with modified current reconstruction for low-speed sensorless control of IPMSMs with a single DC-link current sensor," *IEEE Access*, vol. 7, pp. 136137–136147, 2019.

[30] L. Tian, Z. Wang, Q. Yu, C. Tang, and H. Zhang, "Current reconstruction by one-step compensation for permanent magnet synchronous motor with fixed sampling interval in position sensorless control," *IEEE Trans. Ind. Electron.*, vol. 70, no. 1, pp. 200–210, Jan. 2023.

[31] Y. Wang, Y. Xu, and J. Zou, "Sliding-mode sensorless control of PMSM with inverter nonlinearity compensation," *IEEE Trans. Power Electron.*, vol. 34, no. 10, pp. 10206–10220, Oct. 2019.